

DINO in the Room: Leveraging 2D Foundation Models for 3D Segmentation

Karim Abou Zeid^{1,*} Kadir Yilmaz^{1,*} Daan de Geus^{1,2} Alexander Hermans¹
 David Adrian³ Timm Linder³ Bastian Leibe¹
¹RWTH Aachen University ²Eindhoven University of Technology ³Bosch Center for AI
vision.rwth-aachen.de/DITR

Abstract

Vision foundation models (VFMs) trained on large-scale image datasets provide high-quality features that have significantly advanced 2D visual recognition. However, their potential in 3D vision remains largely untapped, despite the common availability of 2D images alongside 3D point cloud datasets. While significant research has been dedicated to 2D–3D fusion, recent state-of-the-art 3D methods predominantly focus on 3D data, leaving the integration of VFMs into 3D models underexplored. In this work, we challenge this trend by introducing DITR, a simple yet effective approach that extracts 2D foundation model features, projects them to 3D, and finally injects them into a 3D point cloud segmentation model. DITR achieves state-of-the-art results on both indoor and outdoor 3D semantic segmentation benchmarks. To enable the use of VFMs even when images are unavailable during inference, we further propose to distill 2D foundation models into a 3D backbone as a pretraining task. By initializing the 3D backbone with knowledge distilled from 2D VFMs, we create a strong basis for downstream 3D segmentation tasks, ultimately boosting performance across various datasets. Code will be made available upon acceptance.

1. Introduction

We need to talk about the elephant DINO in the room.

Current state-of-the-art 3D semantic segmentation models use specialized 3D backbones, which are trained from scratch [7, 56, 58]. In contrast, for the highly related task of image segmentation, the current paradigm is to use 2D backbones initialized with pretrained weights of strong vision foundation models [5, 11, 22, 23, 33, 41, 43, 64] (VFMs). These VFMs are predominantly trained in a self-supervised manner on large-scale image datasets, enabling strong generalization capabilities. However, current 3D datasets [1, 3, 4, 8, 44, 50, 67] are orders of magnitude

*Equal contribution. The order is determined by a last-minute coin flip.

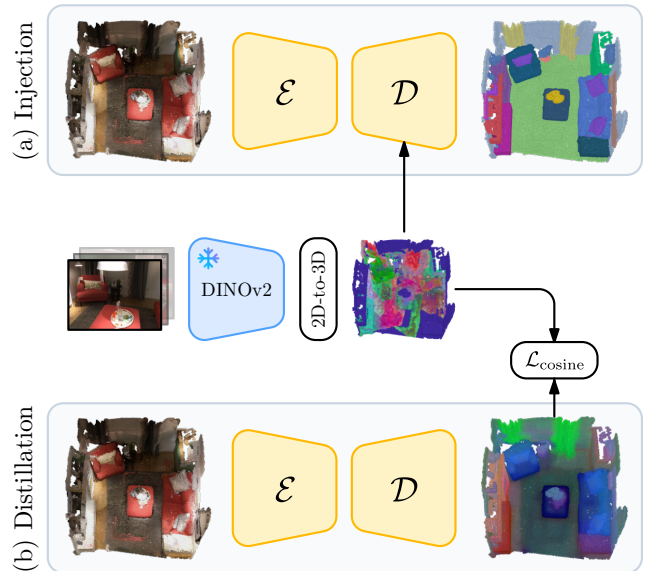


Figure 1. **DINO in the room (DITR)**. We present a simple approach to (a) inject or (b) distill DINOv2 features into 3D semantic segmentation models that yields state-of-the-art results across indoor and outdoor 3D benchmarks.

smaller than their 2D counterparts [46, 47]. As a result, generalist 3D foundation models have yet to emerge. Interestingly, though, we observe that 3D point cloud data is often accompanied by corresponding 2D images [4, 8, 44, 50]. This raises the question: can we leverage the power of 2D foundation models for 3D segmentation?

For most 3D point clouds, corresponding images are typically available due to the process with which this data is captured. In indoor scenarios, a scene is captured with RGB or RGB-D cameras as a video sequence and a colored point cloud is formed via 3D reconstruction [8, 44]. As a result, the data inherently includes 2D images, and correspondences between images and point clouds are obtained as part of data preprocessing. In outdoor scenarios, 3D street scenes are typically captured with LiDAR scanners mounted on vehicles that are often also equipped with cameras, providing corresponding 2D images [3, 4, 50]. De-

spite the availability of these images, current state-of-the-art methods for both indoor and outdoor 3D semantic segmentation predominantly focus on 3D data [24, 58, 59, 63]. While 2D–3D fusion has been investigated with moderate success [2, 20, 42, 51, 65], existing works have thus far not capitalized on the existence of semantically rich VFMs.

In this paper, we challenge the current paradigm and claim that VFMs can, as they did in 2D, enrich 3D models with generalist features that are not easily learned from the 3D data. We verify this by showing that a simple combination of a VFM and a state-of-the-art 3D segmentation model [58] significantly outperforms existing models, achieving new state-of-the-art results on several benchmarks. Concretely, we take a frozen DINOv2 ViT [33] and extract image features that correspond to the points in the associated point cloud. Next, we inject these 2D features into their corresponding points in the decoder of the 3D backbone. Then, we train this model for the regular segmentation objective, resulting in the 2D-to-3D injection approach (see Fig. 1 (a)). Notably, the segmentation performance improves significantly, while only using unlabeled images. Especially for indoor datasets with many semantic classes and for outdoor datasets that provide 360° camera coverage, this setup outperforms the 3D-only baseline on public leader boards by large margins, *i.e.*, +7.1 mIoU on ScanNet200 [44] and +2.4 mIoU on nuScenes [4]. We call this approach *DINO In The Room* (DITR).

Moreover, we show that even if images are not available during inference, it is still possible to utilize features from the same frozen DINOv2 model to enhance segmentation performance through *distillation* [15]. Specifically, we take 3D point cloud datasets that have corresponding images and teach a 3D student model to output features aligned with those extracted from a DINOv2 teacher model, using a distillation objective (see Fig. 1 (b)). Subsequently, the distilled student model can simply be fine-tuned for 3D segmentation in a regular fashion, without requiring corresponding images, and thus without causing any overhead during inference. This distillation pretraining enables the 3D model to capture the semantic richness of 2D foundation models without requiring any labeled data, effectively using them as distillation targets instead of semantic labels. Furthermore, it allows pretraining across multiple datasets without adjusting for dataset-specific semantic label sets, as the target feature space remains consistent. With this setup, we observe consistent improvements on all datasets compared to random initialization. On SemanticKITTI [3], where there is only a single image per 3D LiDAR scan, and on S3DIS [1], where camera views are sparser, this distillation setup even outperforms DITR. We call this approach *Distill DITR* (D-DITR).

Altogether, these results highlight the significant yet underexplored potential of VFMs for 3D tasks. We hope that

our findings will promote the use of VFMs in 3D scene understanding and encourage further research into this direction. Additionally, we note that while we focus on DINOv2 in this paper, as it represents the current strongest VFM, we anticipate that the general setup can leverage even stronger models that we expect to see in the future. Therefore, we recommend that whenever corresponding images are available, they should be used to complement 3D segmentation models, preferably using injection and otherwise using distillation.

In summary, our contributions are as follows:

- We show that injection of DINOv2 features from 2D images into a 3D model can significantly improve the segmentation performance, achieving new state-of-the-art results on multiple indoor and outdoor datasets.
- We demonstrate that DINOv2 can also act as a teacher for pretraining backbones of 3D models through distillation, surpassing the performance of existing unsupervised pretraining methods.

2. Related Work

3D Semantic Segmentation. Despite architectural differences, most 3D backbones for dense tasks such as segmentation follow a U-Net-like hierarchical encoder–decoder design with skip connections. Early methods apply point-wise fully-connected layers [38, 39], or continuous 3D convolutions [35, 53] to capture local geometric patterns. Later, MinkUNet [7] significantly improves efficiency and accuracy by voxelizing point clouds and utilizing sparse 3D convolutions [13]. Following the success of Vision Transformers [10], attention mechanisms have been increasingly adopted for 3D segmentation, although their quadratic computational complexity poses challenges for large-scale scenes. To address this, several methods [26, 55, 56, 58, 62, 66] restrict attention to local neighborhoods, where points are subsampled and aggregated hierarchically across multiple layers. Most recently, Point Transformer V3 (PTv3) [58] employs space-filling curves to map 3D point clouds into 1D sequences, effectively preserving the local neighborhood structure while significantly simplifying and accelerating local attention computations. PTv3 achieves state-of-the-art performance across both indoor and outdoor datasets. In this work, we enhance PTv3 with VFM features to further improve performance.

2D–3D Fusion. Significant research has been dedicated to fusing 2D and 3D information for 3D segmentation. Existing fusion methods are often designed with a domain-specific focus, addressing either indoor or outdoor scenes.

Indoor fusion methods exploit multi-view information from RGB-D videos, as points are visible from multiple angles. Kundu *et al.* [25] render 2D images and their corresponding ground-truth labels from 3D mesh reconstruc-

tions to train a 2D segmentation model. During inference, resulting multi-view 2D predictions are aggregated in 3D space. Other approaches leverage 2D segmentation annotations provided by the 3D datasets [8], either by pretraining 2D networks [21] or by jointly training 2D and 3D networks with interactions between them [17]. Recent methods use dedicated architectures for 2D–3D fusion, introducing either an aggregation module that selectively fuses 2D features into a 3D backbone [42], or a unified 2D–3D model with alternating 2D–3D layers enabling multi-stage fusion of multi-modal information [20].

Outdoor fusion methods combine appearance-based 2D features with geometric LiDAR features for segmentation. Some methods [51, 69] project LiDAR points to the image plane and jointly train a camera and a LiDAR network, while simultaneously aligning their features. Other approaches introduce more sophisticated fusion mechanisms, such as selecting semantically relevant 2D regions for each point via local attention modules [65], or establishing 2D–3D correspondences through joint spatial and semantic reasoning [28]. Finally, 4D-Former [2] explores 2D–3D fusion for LiDAR segmentation and tracking, integrating 2D features into a 3D backbone at multiple stages.

While these works effectively use 2D information for 3D segmentation, we observe that the community has not yet identified or leveraged the power of VFMs. In this work, we demonstrate that a simple injection of features from a strong 2D model—DINOv2 [33]—into a 3D model allows for a significantly better segmentation performance, obtaining new state-of-the-art results. Moreover, DITR is the first fusion approach shown to be effective for both indoor and outdoor scenes, highlighting its general applicability.

2D–3D Distillation. Recent methods have explored various strategies to distill 2D representations into 3D backbones for enhanced representation learning in LiDAR point clouds. Yan *et al.* [60] propose a joint training framework, where a 3D model is trained for both 3D segmentation and alignment with a 2D model, improving learned 3D representations. Several approaches apply contrastive learning either on super-points and super-pixels generated by pre-trained 2D backbones [29, 45], or on prototypes created in both the 2D and 3D domains [6]. Others [31, 32] propose new contrastive loss functions to address the issue of contrasting semantically similar regions, and conduct extensive experiments with linear probing or limited-data setups. Recently, ScaLR [37] studies the effects of the size of the 3D backbone, 2D backbone, and the dataset in the image-to-LiDAR distillation setup, and shows that scaling the models and pretraining on diverse datasets is crucial for distillation. Interestingly, while these existing methods have leveraged image-to-LiDAR distillation for zero-shot 3D segmentation and linear probing with success, they have not demonstrated that VFM distillation allows for more accurate fine-tuning.

In this work, we demonstrate that a simple distillation setup using a strong VFM enables accurate image-free inference with DITR. Moreover, while related works focus on LiDAR data, our D-DITR distillation setup is not only effective in combination with LiDAR data, but also for indoor scenes.

Orthogonal to other distillation methods, there is also a line of work that distills specific capabilities from VFMs. Peng *et al.* [36] distill language-aligned CLIP [41] features from multiple views for 3D open-vocabulary segmentation. Other approaches [18, 34] use projected SAM [23] segmentation masks as pseudo ground-truth labels to train class-agnostic 3D segmentation models. Although these approaches also distill from 2D foundation models, they focus on obtaining task-specific capabilities in a zero-shot setting to avoid the reliance on 3D segmentation annotations. In contrast, we use distillation to obtain a pretrained 3D model that extracts semantically rich point features, which can then be fine-tuned for 3D segmentation and, in principle, other 3D tasks as well.

3. Method

We propose two variants of DITR for 3D semantic segmentation: an *injection* approach that uses 2D features from DINOv2 [33] during training and inference, and D-DITR, a *distillation* approach that aligns 3D features with DINOv2 features during a pretraining phase, which can be followed by image-free fine-tuning on a specific dataset. In the following, we describe both variants in detail.

3.1. Injection

In many modern 3D datasets, images from calibrated cameras are provided alongside the point clouds [1, 3, 4, 8, 50]. We leverage these images to inject semantically rich 2D features into the 3D backbone. An overview of this process is shown in Fig. 2: we first map 3D points to their corresponding pixels to extract associated DINOv2 features (2D-to-3D Mapping), then inject these features into the skip connections of the 3D backbone’s decoder (3D Feature Fusion).

2D-to-3D Mapping. Let $\mathcal{P} = \{\mathbf{p}_i \in \mathbb{R}^3\}_{i=1}^N$ be a 3D point cloud of N points, and assume a collection of K calibrated cameras, $\{(\mathbf{I}_k, \mathbf{K}_k, \mathbf{T}_k)\}_{k=1}^K$. Each camera has intrinsics \mathbf{K}_k and world-to-camera extrinsics \mathbf{T}_k , with \mathbf{I}_k denoting its captured image of resolution $H \times W$. We feed each 2D image \mathbf{I}_k into a frozen DINOv2 ViT [10], obtaining patch-level embeddings $\mathbf{F}_k \in \mathbb{R}^{\frac{H}{P} \times \frac{W}{P} \times D_{2D}}$, where P is the patch size and D_{2D} is the feature dimension. For each point \mathbf{p}_i , we transform it into the k -th camera space as $\mathbf{q}_i^k = \mathbf{T}_k(\mathbf{p}_i, 1)$ and multiply by the intrinsics \mathbf{K}_k to obtain homogeneous pixel coordinates $(x_i^k, y_i^k, z_i^k) = \mathbf{K}_k \mathbf{q}_i^k$. The pixel coordinates are then given by $(u_i^k, v_i^k) = (x_i^k/z_i^k, y_i^k/z_i^k)$. We consider \mathbf{p}_i visible in the k -th image if $u_i^k \in [0, W)$, $v_i^k \in [0, H)$ and the depth z_i^k is positive (view-frustum

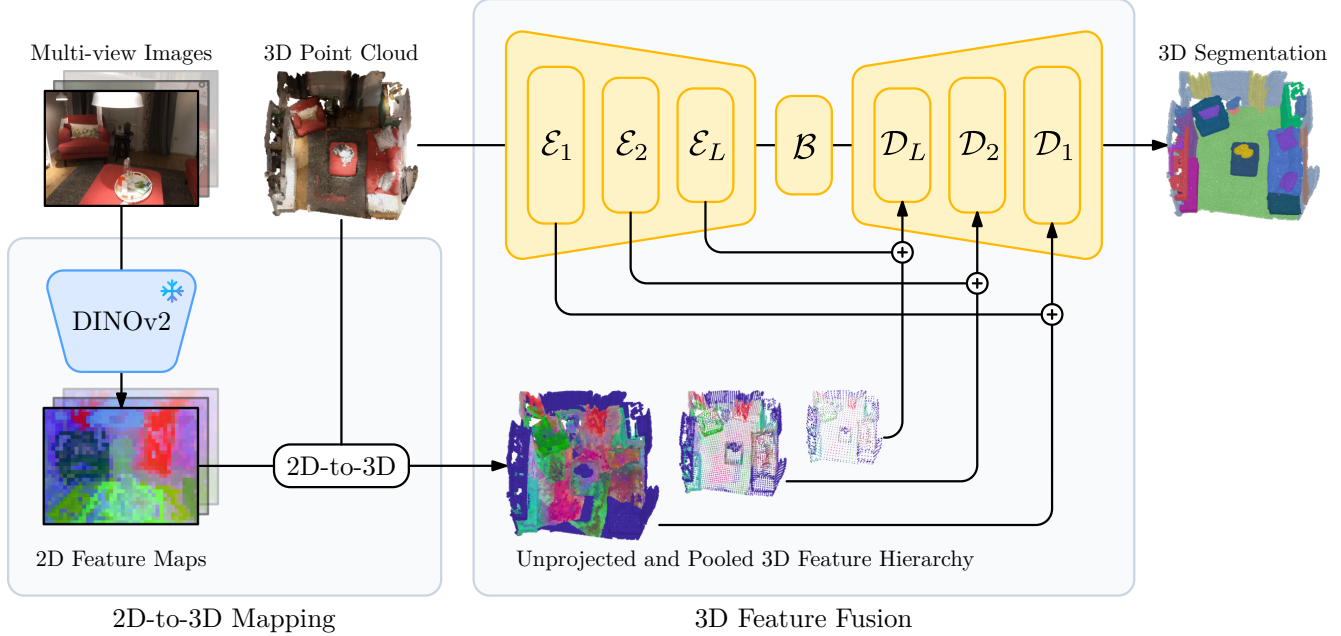


Figure 2. **DITR architecture overview.** We extract 2D image features from a frozen DINOv2 [33] model \square and unproject them (2D-to-3D) onto the 3D point cloud. The unprojected features are subsequently max-pooled to create a multi-scale feature hierarchy. The raw point cloud is fed through a 3D backbone \square and the unprojected image features are added to the skip connection between the encoder \mathcal{E}_l and decoder \mathcal{D}_l block on each level. The model is then trained with the regular segmentation loss.

culling). If \mathbf{p}_i is visible in the k -th image, we determine the corresponding patch index as

$$(\hat{u}_i^k, \hat{v}_i^k) = \left(\left\lfloor \frac{u_i^k}{P} \right\rfloor, \left\lfloor \frac{v_i^k}{P} \right\rfloor \right),$$

and assign the corresponding feature from the 2D feature map \mathbf{F}_k to \mathbf{p}_i . If \mathbf{p}_i is visible in multiple images, we randomly select one of them to provide the feature. Otherwise, if \mathbf{p}_i is not visible in any image, we assign an all-zero feature vector. Empirically, we find that directly assigning the feature from the frozen 2D feature map \mathbf{F}_k at patch index $(\hat{u}_i^k, \hat{v}_i^k)$ yields better results than bilinearly interpolating features from \mathbf{F}_k at the pixel coordinates (u_i^k, v_i^k) . Also, aggregating from multiple 2D feature maps resulted in inferior performance compared to random selection.

3D Feature Fusion. Because point clouds are unstructured, common 3D backbones [7, 58, 68] voxelize the input, keeping only one point per voxel, thereby reducing \mathcal{P} to \mathcal{P}' with $M \leq N$ points. These backbones typically follow a U-Net-like encoder–decoder architecture, processing \mathcal{P}' at multiple spatial resolution levels $l \in \{1, \dots, L\}$. At each encoder level, a pooling layer downsamples the point features to a coarser spatial resolution. Formally, let $\mathbf{X}_l^\mathcal{E} \in \mathbb{R}^{M_l \times D_l}$ denote the output of the l -th level encoder block \mathcal{E}_l , where $l = 1$ is the finest (original) resolution with $M_1 = M$. After the encoder and the bottleneck \mathcal{B} , the decoder upsamples and refines these features back toward the original resolution, yielding $\mathbf{X}_l^\mathcal{D}$ as the output of each de-

coder block \mathcal{D}_l . To simplify notation, we define $\mathbf{X}_{L+1}^\mathcal{D}$ to be the output of the bottleneck \mathcal{B} .

To incorporate DINOv2 features, we first use the previously described assignment to gather point-wise features $\mathbf{X}^{2D} \in \mathbb{R}^{M \times D_{2D}}$ for the points in \mathcal{P}' from the 2D feature maps \mathbf{F}_k . Then, to mirror the spatial structure of the decoder features $\mathbf{X}_l^\mathcal{D}$ across different levels, we repeatedly apply max pooling to \mathbf{X}^{2D} , obtaining features \mathbf{X}_l^{2D} for each level l . In the decoder, features from the encoder ($\mathbf{X}_l^\mathcal{E}$) and unpooled features from the previous decoder level ($\uparrow \mathbf{X}_{l+1}^\mathcal{D}$) are combined via skip connections. In DITR, we additionally inject \mathbf{X}_l^{2D} into these skip connections. Specifically, the fused input to the l -th decoder block \mathcal{D}_l becomes

$$\underbrace{f_l^\mathcal{D}(\uparrow \mathbf{X}_{l+1}^\mathcal{D})}_{\text{prev. dec. block}} + \underbrace{f_l^\mathcal{E}(\mathbf{X}_l^\mathcal{E})}_{\text{skip connection}} + \underbrace{f_l^{2D}(\mathbf{X}_l^{2D})}_{\text{DINOv2}},$$

where $+$ denotes element-wise addition, and each f_i is a linear projection into the decoder’s feature dimension followed by batch normalization [19] and GELU [14]. Finally, the output $\mathbf{X}_1^\mathcal{D}$ of the last decoder block yields per-point features for \mathcal{P}' , which are passed through a linear segmentation head to produce class logits.

3.2. Distillation

While injecting DINOv2 features directly into the 3D backbone can significantly boost segmentation performance, relying on calibrated images at inference time may be restrictive in certain real-world scenarios. To address situations

where only 3D data can be used at test time, we propose a distillation scheme (D-DITR) to transfer knowledge from the frozen 2D encoder into a pure 3D model.

Pretraining via 2D-to-3D Alignment. During pretraining, we first match 3D points to 2D patches and assign per-point DINOv2 features \mathbf{X}^{2D} as described in Sec. 3.1. We then feed only the point cloud into the 3D backbone, but instead of predicting segmentation logits, the network’s final linear layer regresses the DINOv2 features. For each point \mathbf{p}_i , we denote the predicted feature by $\mathbf{x}_i^{\text{pred}}$ and the corresponding DINOv2 target feature by \mathbf{x}_i^{2D} . We minimize the following cosine similarity loss [36], averaged over all visible points:

$$\mathcal{L}_{\text{cosine}} = \frac{1}{|\mathcal{V}|} \sum_{i \in \mathcal{V}} \left[1 - \frac{\mathbf{x}_i^{\text{pred}} \cdot \mathbf{x}_i^{2D}}{\|\mathbf{x}_i^{\text{pred}}\| \|\mathbf{x}_i^{2D}\|} \right], \quad (1)$$

where \mathcal{V} is the set of indices of points visible in at least one camera. This distillation pretraining encourages the 3D backbone to replicate the semantically rich representations of DINOv2, which capture fine-grained details without being constrained by the coarse granularity of traditional semantic segmentation annotations. An overview of the distillation setup is shown in Fig. 1 (b).

Image-free Inference. After pretraining, we discard the linear regression head and replace it with the standard segmentation head. The pretrained model can then be finetuned on any 3D segmentation dataset without requiring image features. The final model thus makes predictions based on 3D data only, yet benefits from the semantic knowledge transferred from strong 2D models.

Multi-Dataset Training. A key advantage of our 2D-to-3D distillation approach is that it does not require any annotated data. It only requires aligned 2D and 3D inputs. This enables us to combine multiple unannotated point cloud datasets under a single distillation objective, where each point simply regresses to its corresponding DINOv2 feature. Following prior multi-dataset work [59], we maintain separate batch-normalization layers per dataset, which empirically leads to more stable training.

4. Experiments

4.1. Datasets

We evaluate our method on well-established 3D indoor and outdoor segmentation benchmarks. For indoor segmentation, we select ScanNet [8], ScanNet200 [44], and S3DIS [1]. All three datasets consist of colored point clouds and their corresponding RGB-D frames. For outdoor segmentation, we select nuScenes [4], SemanticKITTI [3], and Waymo [50]. nuScenes provides six cameras with combined 360° surround coverage and captures point clouds using a 32-beam LiDAR sensor. Waymo offers five cameras covering the front and sides, and uses a 64-beam main

LiDAR along with four short-range LiDAR sensors, resulting in a dense point cloud. SemanticKITTI also uses a 64-beam LiDAR, resulting in a density similar to Waymo, but includes only a single front-facing camera.

4.2. Implementation Details

We use PTv3 [58] as our 3D backbone, as it is the state-of-the-art model for 3D semantic segmentation across both indoor and outdoor datasets. Unless stated otherwise, we retain the default architecture and learning hyperparameters of PTv3 to ensure fair comparison; additional details are provided in the supplementary material. For all datasets, we adhere to standard evaluation protocols and metrics. Reproducing PTv3 results on the S3DIS¹ and SemanticKITTI² datasets has been notoriously hard for the community. Therefore, we also report our reproduced results as a reference.

For outdoor scenarios, we observe large performance improvements with larger DINOv2 variants and thus we opt for the largest ViT-g model. For indoor datasets, the ViT-L and ViT-g variants yield comparable results (as shown in Tab. 9). Consequently, we choose the ViT-L model to optimize resource efficiency, enabling the use of more images while remaining within GPU memory constraints.

During both training and inference on outdoor scenes, we use all available camera views: one for SemanticKITTI, five for Waymo, and six for nuScenes. These camera views appear in a consistent orientation with respect to the LiDAR sensor and can be assumed always to be present for all scans. For the indoor datasets, the number of RGB-D frames per scene can vary tremendously and always surpasses the number of frames we can effectively process with the available GPU memory. Therefore, unless specified otherwise, we select 10 uniformly sampled, temporally equidistant frames from each RGB-D video during inference, while randomly sampling 10 views per scene during training to enhance data diversity. Since DINOv2 is pretrained at a maximum resolution of 518×518 , we resize input images to maintain a similar amount of patches while preserving aspect ratio [54]. Further details are provided in the supplementary material.

4.3. Quantitative Results

Injection. DITR achieves state-of-the-art semantic segmentation results across both indoor and outdoor datasets as shown in Tabs. 1 and 2. In particular, we outperform all previous 2D–3D fusion approaches, even though these methods either focus on indoor or outdoor settings. On the ScanNet200 hidden test set, we see an improvement of +7.1 mIoU, showing that image feature injection is especially beneficial for harder segmentation tasks with many

¹<https://github.com/Pointcept/Pointcept/issues/154>

²<https://github.com/Pointcept/Pointcept/issues/186>

Method	ScanNet		ScanNet200		S3DIS
	Val	Test	Val	Test	Area5
ST [26]	74.3	73.7	—	—	72.0
PTv1 [66]	70.6	—	27.8	—	70.4
PointNeXt [40]	71.5	71.2	—	—	70.5
MinkUNet [7]	72.2	73.6	25.0	25.3	65.4
OctFormer [55]	75.7	76.6	32.6	32.6	—
Swin3D [62]	76.4	—	—	—	72.5
PTv2 [56]	75.4	74.2	30.2	—	71.6
PTv3 [58]	77.5	77.9	35.2	37.8	73.4 [†]
↳ reproduced	76.8	—	35.4	—	72.1
DVA [42]	71.0	—	—	—	67.2
BPNNet [17]	73.9	74.9	—	—	—
DMF-Net [61]	75.6	75.2	—	—	—
VMVF [25]	76.4	74.6	—	—	—
ODIN [20]	77.8	74.4	40.5	36.8	68.6
DITR	80.5	79.7	41.2	44.9	74.1

Table 1. **Indoor semantic segmentation results (mIoU)**. We obtain state-of-the-art results on all datasets. We compare against both 3D-only (top) and 2D–3D fusion methods (bottom). [†]: Uses a smaller point patch size and relative positional encoding.

Method	nuScenes		Sem.KITTI		Waymo
	Val	Test	Val	Test	Val
MinkUNet [7]	73.3	—	63.8	—	65.9
SPVNAS [52]	77.4	—	64.7	66.4	—
Cylinder3D [68]	76.1	77.2	64.3	67.8	—
SphereFormer [27]	78.4	81.9	67.8	74.8	69.9
PTv2 [56]	80.2	82.6	70.3	72.6	70.6
PTv3 [58]	80.4	82.7	70.8	74.2	71.3
↳ reproduced	79.9	—	68.3	—	71.5
4D-Former [2]	78.9	80.4	66.3	—	—
2DPASS [60]	79.4	80.8	69.3	72.9	—
MSeg3D [28]	80.0	81.1	66.7	—	69.6
LCPS [65]	80.5	78.9	67.5	62.8	—
DITR	84.2	85.1	69.0	74.4	73.3

Table 2. **Outdoor semantic segmentation results (mIoU)**. We obtain state-of-the-art results on datasets with full camera coverage: nuScenes and Waymo. We compare against both 3D-only (top) and 2D–3D fusion methods (bottom).

classes. Among the outdoor datasets, only on the SemanticKITTI dataset DITR falls slightly behind the top-performing methods. Given that this dataset provides only a single front-facing camera, moderate improvements are to be expected. However, nuScenes stands out with a +4.3 mIoU improvement on the validation set. This could be caused by the fact that the nuScenes point clouds are sparser than those of the other datasets, thus resulting in a stronger boost from the dense image features.

Distillation. For distillation pretraining, we explore two

Method	ScanNet	ScanNet200	S3DIS
PTv3 [58]	77.5	35.2	73.4 [†]
↳ reproduced	76.8	35.4	72.1
D-DITR	78.6	37.2	—
D-DITR (multi-dataset)	79.2	37.7	75.0

Table 3. **Indoor distillation results (mIoU)**. We evaluate models pretrained and fine-tuned on the same datasets, as well as one pretrained on ScanNet and Structured3D. All models outperform the randomly initialized PTv3 baseline. [†]: Uses a smaller point patch size and relative positional encoding.

Method	nuScenes	Sem.KITTI	Waymo
PTv3 [58]	80.4	70.8	71.3
↳ reproduced	79.9	68.3	71.5
D-DITR	80.9	—	71.6
D-DITR (multi-dataset)	80.7	69.8	72.1

Table 4. **Outdoor distillation results (mIoU)**. We evaluate models pretrained and fine-tuned on the same datasets, as well as one pretrained on all three. In all cases, our models outperform the randomly initialized PTv3 baseline. Sem.KITTI is excluded from single-dataset pretraining due to its single-camera setup.

settings: (1) pretraining on individual datasets and fine-tuning on the same dataset to show the effectiveness of VFM features as distillation targets, and (2) joint pretraining on multiple datasets. In the indoor multi-dataset distillation case, we jointly pretrain on ScanNet and Structured3D [67] and for the outdoor case we use nuScenes, SemanticKITTI, and Waymo. We exclude S3DIS from pretraining due to its smaller size and instead use it to assess generalization on an unseen dataset. The results are presented in Tab. 3 and Tab. 4 as D-DITR. Single-dataset distillation yields consistent improvements over the PTv3 baseline, demonstrating the effectiveness of DINOv2 distillation. The use of multi-dataset distillation further improves the results. In indoor datasets, distillation pretraining significantly improves the segmentation performance, with gains of +2.4 mIoU on ScanNet, +2.3 mIoU on ScanNet200 and +2.9 mIoU on S3DIS over the state-of-the-art 3D baseline. The improvement on S3DIS is particularly interesting, indicating that the distilled features can generalize to unseen datasets. For outdoor datasets, D-DITR also produces consistent improvements over the baseline. In particular, the distillation approach yields notable gains on SemanticKITTI, and even surpasses the *injected* DITR model (see Tab. 2). This indicates that even when images are not available, or compute constraints do not allow for the computation of DINOv2 features during inference, D-DITR can utilize these strong 2D features during pretraining for enhanced segmentation.

Fig. 3 shows feature predictions of D-DITR prior to fine-tuning, on several indoor and outdoor scenes. When compared to the ground-truth segmentations, objects are clearly

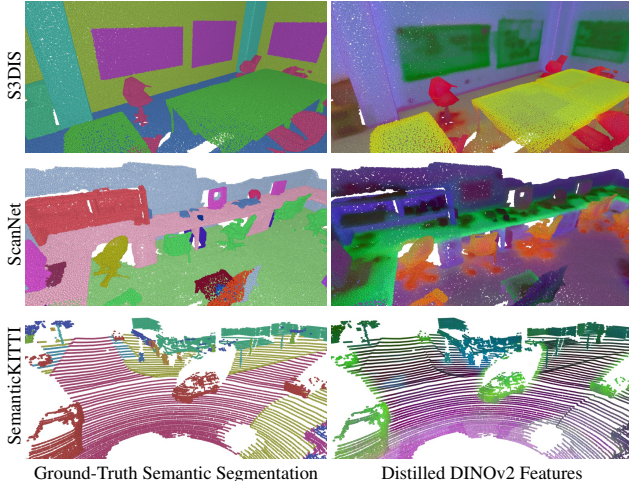


Figure 3. **D-DITR distillation.** We show PCA projected features from D-DITR after distillation. Many objects in the ground-truth segmentation are clearly separable in the predicted features, indicating the value of DINOv2 features for 3D segmentation. The colors are not expected to match, but color “clusters” should align.

% Data	Scratch	CSC [16]	MSC [57]	PPT [59]	D-DITR
1 %	26.0	28.9 ^{†2.9}	29.2 ^{†3.2}	31.3 ^{†5.3}	34.1 ^{†8.1}
5 %	47.8	49.8 ^{†2.0}	50.7 ^{†2.9}	52.2 ^{†4.4}	56.6 ^{†8.8}
10 %	56.7	59.4 ^{†2.7}	61.0 ^{†4.3}	62.8 ^{†6.1}	65.2 ^{†8.5}
20 %	62.9	64.6 ^{†1.7}	64.9 ^{†2.0}	66.4 ^{†3.5}	68.3 ^{†5.4}
100 %	72.2	73.8 ^{†1.6}	75.3 ^{†3.1}	75.8 ^{†3.6}	76.2 ^{†4.0}

Table 5. **ScanNet limited reconstructions benchmark using the MinkUNet [7] 3D backbone.** All methods perform pretraining on unannotated raw data, followed by segmentation fine-tuning on fixed labeled subsets of ScanNet. The baseline is a MinkUNet trained from scratch.

separable by color, even when visualizing only the first three principal components of the high-dimensional feature space. This further indicates the value of DINOv2 features for 3D semantic segmentation.

ScanNet Data Efficient Benchmark. To demonstrate that D-DITR is also effective in label-scarce settings, we use the ScanNet limited reconstructions benchmark and show results for different percentages of available data during fine-tuning in Tab. 5. For this setting, we use MinkUNet [7] as the student model to compare with previous unsupervised approaches in a consistent setting. Similar to CSC [16], we use additional unlabeled images. D-DITR outperforms all previous unsupervised pretraining approaches in all settings. The gap is even larger when a small percentage of data is available during fine-tuning. Overall, this experiment shows that this distillation approach can be applied to other commonly used 3D backbones, providing a strong supervision signal compared to raw 3D data.

Method	ScanNet200		SemanticKITTI	
	Visible	Invisible	Visible	Invisible
PTv3 [58]	35.2	34.5	68.5	68.1
DITR	41.5	39.7	71.6	68.3

Table 6. **Performance on visible and invisible points.** We compare the segmentation performance of points visible in at least one image to those that are never visible. For SemanticKITTI, only 18.9 % of labeled points are visible.

Image selection		ScanNet200			nuScenes	
# Images	Method	mIoU ₆	mIoU ₁₀	% Vis.	mIoU	% Vis.
0	eq.dist.	32.8	31.8	0.0	37.5	0.0
1	eq.dist.	36.5	35.7	9.8	50.9	11.2
3	eq.dist.	38.2	38.0	24.6	72.7	40.5
6	eq.dist.	39.2	40.1	41.7	83.1	77.0
10	eq.dist.	39.9	41.2	56.7	—	—
6	random	38.6	38.4	37.0	—	—
10	random	39.2	40.5	49.5	—	—

Table 7. **Number of images and image selection strategy during inference.** We compare two inference-time image selection methods: random selection and temporally-equidistant frame selection (eq.dist.). For ScanNet200, we compare models trained on 6 (mIoU₆) or 10 random images (mIoU₁₀). For nuScenes, the model is trained using all six camera views. During inference, we use different subsets of cameras: no camera; the front camera alone; the front, back-left, and back-right cameras; all six cameras.

Visibility vs. Performance. To better understand the source of the performance improvement, in Tab. 6, we compare the performance of DITR and the baseline on visible and invisible points separately. DITR shows a notable improvement on visible points for both the ScanNet200 and SemanticKITTI datasets. Moreover, it still outperforms the PTv3 baseline even on invisible points. The substantial improvement on ScanNet200 suggests that the model captures global context from the 2D features, aiding the segmentation of invisible regions.

In Tab. 7, we analyze the impact of varying the number of images and the image selection strategy during inference while using the same trained model. For ScanNet200, we evaluate two models, one trained with 6 images per scene and another with 10 to evaluate the impact of the number of training images. For nuScenes, we only evaluate a model trained on all available images. On ScanNet200, the model trained with 6 images benefits from seeing more images during inference than during training and performs better than the one trained with 10 images when fewer images are used during inference. Furthermore, both models demonstrate robustness to seeing fewer images during inference, with performance degrading gracefully as they are trained with randomly selected images. However, on nuScenes, the model always receives the full surrounding visual context during training. As a result, the performance degrades sig-

Injection point	ScanNet200	nuScenes
<i>None</i> (i.e. PTV3 [58])	35.2	79.9
Before segmentation head	37.6	82.5
Before first encoder layer	40.1	82.3
Decoder (last block)	40.1	82.7
Decoder (all blocks) (i.e. DITR)	41.2	83.1
Class tokens only	37.4	79.4

Table 8. **Comparison of different injection points.** We add the image features into the PTV3 model at different points throughout the network. All experiments use the DINOv2-L backbone.

nificantly when frames are missing during inference. Finally, on ScanNet200, we also show the effectiveness of using temporally-equidistant images during inference, resulting in higher point coverage and consistently outperforming the random image selection.

Resource Usage. We assess the runtime impact of DITR, compared to the PTV3 baseline without additional fusion of 2D features. On ScanNet200, using a ViT-L DINOv2 backbone and 10 camera views, training time increases from 12 to 15 hours using two H100 GPUs. The average per-scene inference latency increases from 41 to 76 ms, while the required GPU memory increases from 1.4 to 5.6 GiB (using a single H100 GPU for inference). Although this is a limitation of DITR, we note that these inference penalties do not apply to D-DITR as the architecture remains unchanged.

4.4. Ablation Study

Injection Location Ablation. Tab. 8 compares different methods to inject image features into the 3D backbone. By default, we inject the DINOv2 features into all decoder blocks, yielding the strongest performance across the board. Injecting the features only at the last layer of the decoder is still a fairly strong option, albeit slightly worse. We then look at two other extremes: only injecting them directly prior to the segmentation head, or directly before the first encoder layer, after the points have been projected into a higher dimension. While both configurations improve the performance compared to the baseline, the late fusion approach yields considerably smaller gains on ScanNet200. As the primary computational overhead stems from the computation of VFM features, the location and frequency of injection into the backbone have negligible additional impact on efficiency. Thus, we recommend adding 2D features to all decoder layers.

Tab. 6 showed that DITR even achieves significant improvements on invisible points, suggesting that it might leverage additional features as a kind of global context. To assess this, we also experiment with injecting the class tokens for each image directly into the attention blocks of PTV3. While this does yield a small boost in indoor scenarios, it makes almost no difference in the outdoor case, and

Image backbone		ScanNet200	nuScenes
Pretraining	Model		
—	<i>None</i>	35.2	80.4
IN21k [49]	ViT-L	38.2	80.2
AIMv2 [12]	ViT-L	39.1	82.8
SigLIP 2 [54]	ViT-g	38.1	83.6
DINOv2 [33]	ViT-S	38.2	82.8
DINOv2 [33]	ViT-B	40.7	83.0
DINOv2 [33]	ViT-L	41.2	83.1
DINOv2 [33]	ViT-g	40.8	84.2

Table 9. **Injection with different image backbones.** We compare different image backbones and pretraining schemes for DITR.

using the patch features yields considerably better results. Therefore, we did not further pursue class token injection.

Image Backbone Ablation. To assess the impact of the image backbone used to extract 2D features, we experiment with various commonly used image backbones with frozen weights as shown in Tab. 9. When comparing different DINOv2-pretrained ViT models, there is a consistent trend that larger models perform better. We also compare DINOv2 with other pretraining approaches. A standard ViT-L model pretrained on IN21k [9, 49] shows a modest performance improvement in indoor scenarios compared to the DINOv2 baseline, but reduces performance on the outdoor nuScenes dataset. We further evaluate two alternative foundation models, SigLIP 2 [54] and AIMv2 [12], both of which consistently improve performance in both indoor and outdoor settings. These results suggest that strong pretraining, as used in foundation models, is key to achieving consistent gains across diverse environments. They also indicate that our conclusions are not specific to DINOv2 and are likely to hold with future, even more powerful VFMs, which could serve as drop-in replacements within our framework.

5. Conclusion

Even though 3D foundation models might arise in the future, we argue that the DINO in the room is here to stay. Despite the success of 2D foundation models such as DINOv2, comparable models have yet to emerge in 3D, likely due to the scarcity of large-scale datasets. Therefore, we explore how existing 2D foundation models can be leveraged to enhance 3D segmentation performance. While 2D–3D fusion has been an active area of research, the potential of 2D VFMs remains relatively underexplored. With DITR, we demonstrate that even a straightforward injection of frozen VFM features into a 3D backbone can yield significant performance gains. Moreover, this approach is broadly compatible with both existing and most likely also future 3D backbones and VFMs. Even when images are unavailable during inference, our D-DITR distillation pretraining strategy can still provide substantial improvements.

Notably, both DITR and D-DITR require only unlabeled images, making them readily applicable in most scenarios. Thus, we strongly advocate the use of 2D VFMs for 3D scene understanding whenever possible and hope that our findings will encourage more research in this direction.

Acknowledgements. Karim Abou Zeid, Kadir Yilmaz and Alexander Hermans are funded by the project “Context Understanding for Autonomous Systems” by Robert Bosch GmbH. Computations were performed with computing resources granted by RWTH Aachen under projects `rwth1604` and `rwth1730`.

References

- [1] Iro Armeni, Ozan Sener, Amir R Zamir, Helen Jiang, Ioannis Brilakis, Martin Fischer, and Silvio Savarese. 3D Semantic Parsing of Large-Scale Indoor Spaces. In *CVPR*, 2016. 1, 2, 3, 5, 12
- [2] Ali Athar, Enxu Li, Sergio Casas, and Raquel Urtasun. 4DFormer: Multimodal 4D Panoptic Segmentation. In *CoRL*, 2023. 2, 3, 6
- [3] Jens Behley, Martin Garbade, Andres Milioto, Jan Quenzel, Sven Behnke, Cyrill Stachniss, and Jurgen Gall. SemanticKITTI: A Dataset for Semantic Scene Understanding of LiDAR Sequences. In *ICCV*, 2019. 1, 2, 3, 5, 12, 16
- [4] Holger Caesar, Varun Bankiti, Alex H. Lang, Sourabh Vora, Venice Erin Liong, Qiang Xu, Anush Krishnan, Yu Pan, Giancarlo Baldan, and Oscar Beijbom. nuScenes: A Multimodal Dataset for Autonomous Driving. In *CVPR*, 2020. 1, 2, 3, 5, 12, 17, 18, 21
- [5] Mathilde Caron, Hugo Touvron, Ishan Misra, Hervé Jégou, Julien Mairal, Piotr Bojanowski, and Armand Joulin. Emerging Properties in Self-Supervised Vision Transformers. In *ICCV*, 2021. 1
- [6] Haoming Chen, Zhizhong Zhang, Yanyun Qu, Ruixin Zhang, Xin Tan, and Yuan Xie. Building a Strong Pre-Training Baseline for Universal 3D Large-Scale Perception. In *CVPR*, 2024. 3
- [7] Christopher Choy, JunYoung Gwak, and Silvio Savarese. 4D Spatio-Temporal ConvNets: Minkowski Convolutional Neural Networks. In *CVPR*, 2019. 1, 2, 4, 6, 7
- [8] Angela Dai, Angel X. Chang, Manolis Savva, Maciej Halber, Thomas Funkhouser, and Matthias Nießner. ScanNet: Richly-annotated 3D Reconstructions of Indoor Scenes. In *CVPR*, 2017. 1, 3, 5, 12, 14, 15, 19, 20
- [9] Jia Deng, Wei Dong, Richard Socher, Li-Jia Li, Kai Li, and Li Fei-Fei. ImageNet: A large-scale hierarchical image database. In *CVPR*, 2009. 8
- [10] Alexey Dosovitskiy, Lucas Beyer, Alexander Kolesnikov, Dirk Weissenborn, Xiaohua Zhai, Thomas Unterthiner, Mostafa Dehghani, Matthias Minderer, Georg Heigold, Sylvain Gelly, Jakob Uszkoreit, and Neil Houlsby. An Image is Worth 16x16 Words: Transformers for Image Recognition at Scale. In *ICLR*, 2021. 2, 3
- [11] Yuxin Fang, Quan Sun, Xinggang Wang, Tiejun Huang, Xinlong Wang, and Yue Cao. EVA-02: A Visual Representation for Neon Genesis. *Image and Vision Computing*, 149: 105171, 2024. 1
- [12] Enrico Fini, Mustafa Shukor, Xiujun Li, Philipp Dufter, Michal Klein, David Haldimann, Sai Aitharaju, Victor Guilherme Turrissi da Costa, Louis Béthune, Zhe Gan, et al. Multimodal Autoregressive Pre-training of Large Vision Encoders. *arXiv preprint arXiv:2411.14402*, 2024. 8
- [13] Benjamin Graham, Martin Engelcke, and Laurens Van Der Maaten. 3D Semantic Segmentation with Submanifold Sparse Convolutional Networks. In *CVPR*, 2018. 2
- [14] Dan Hendrycks and Kevin Gimpel. Gaussian Error Linear Units (GELUs). *arXiv preprint arXiv:1606.08415*, 2016. 4
- [15] Geoffrey Hinton, Oriol Vinyals, and Jeff Dean. Distilling the Knowledge in a Neural Network. *arXiv preprint arXiv:1503.02531*, 2015. 2
- [16] Ji Hou, Benjamin Graham, Matthias Nießner, and Saining Xie. Exploring Data-Efficient 3D Scene Understanding with Contrastive Scene Contexts. In *CVPR*, 2021. 7
- [17] Wenbo Hu, Hengshuang Zhao, Li Jiang, Jiaya Jia, and Tien-Tsin Wong. Bidirectional Projection Network for Cross Dimension Scene Understanding. In *CVPR*, 2021. 3, 6
- [18] Rui Huang, Songyou Peng, Ayca Takmaz, Federico Tombari, Marc Pollefeys, Shiji Song, Gao Huang, and Francis Engelmann. Segment3D: Learning Fine-Grained Class-Agnostic 3D Segmentation without Manual Labels. *ECCV*, 2024. 3
- [19] Sergey Ioffe and Christian Szegedy. Batch Normalization: Accelerating Deep Network Training by Reducing Internal Covariate Shift. In *ICML*, 2015. 4
- [20] Ayush Jain, Pushkal Katara, Nikolaos Gkanatsios, Adam W Harley, Gabriel Sarch, Kriti Aggarwal, Vishrav Chaudhary, and Katerina Fragkiadaki. ODIN: A Single Model for 2D and 3D Segmentation. In *CVPR*, 2024. 2, 3, 6
- [21] Maximilian Jaritz, Jiayuan Gu, and Hao Su. Multi-view PointNet for 3D Scene Understanding. In *CVPR Workshops*, 2019. 3
- [22] Tommie Kerssies, de Geus, Daan, and Gijs Dubbelman. How to Benchmark Vision Foundation Models for Semantic Segmentation? In *CVPR Workshops*, 2024. 1
- [23] Alexander Kirillov, Eric Mintun, Nikhila Ravi, Hanzi Mao, Chloe Rolland, Laura Gustafson, Tete Xiao, Spencer Whitehead, Alexander C. Berg, Wan-Yen Lo, Piotr Dollar, and Ross Girshick. Segment Anything. In *ICCV*, 2023. 1, 3
- [24] Maxim Kolodiaznyi, Anna Vorontsova, Anton Konushin, and Danila Rukhovich. OneFormer3D: One Transformer for Unified Point Cloud Segmentation. In *CVPR*, 2024. 2
- [25] Abhijit Kundu, Xiaoqi Yin, Alireza Fathi, David Ross, Brian Brewington, Thomas Funkhouser, and Caroline Pantofaru. Virtual Multi-view Fusion for 3D Semantic Segmentation. In *ECCV*, 2020. 2, 6
- [26] Xin Lai, Jianhui Liu, Li Jiang, Liwei Wang, Hengshuang Zhao, Shu Liu, Xiaojuan Qi, and Jiaya Jia. Stratified Transformer for 3D Point Cloud Segmentation. In *CVPR*, 2022. 2, 6
- [27] Xin Lai, Yukang Chen, Fanbin Lu, Jianhui Liu, and Jiaya Jia. Spherical Transformer for LiDAR-Based 3D Recognition. In *CVPR*, 2023. 6
- [28] Jiale Li, Hang Dai, Hao Han, and Yong Ding. MSeg3D: Multi-modal 3D Semantic Segmentation for Autonomous Driving. In *CVPR*, 2023. 3, 6

- [29] Youquan Liu, Lingdong Kong, Jun CEN, Runnan Chen, Wenwei Zhang, Liang Pan, Kai Chen, and Ziwei Liu. Segment Any Point Cloud Sequences by Distilling Vision Foundation Models. In *NeurIPS*, 2023. 3
- [30] Ilya Loshchilov and Frank Hutter. Decoupled Weight Decay Regularization. In *ICLR*, 2019. 12
- [31] Anas Mahmoud, Jordan S. K. Hu, Tianshu Kuai, Ali Harakeh, Liam Paull, and Steven L. Waslander. Self-Supervised Image-to-Point Distillation via Semantically Tolerant Contrastive Loss. In *CVPR*, 2023. 3
- [32] Anas Mahmoud, Ali Harakeh, and Steven Waslander. Image-to-Lidar Relational Distillation for Autonomous Driving Data. In *ECCV*, 2024. 3
- [33] Maxime Oquab, Timothée Darcet, Théo Moutakanni, Huy V. Vo, Marc Szafraniec, Vasil Khalidov, Pierre Fernandez, Daniel Haziza, Francisco Massa, Alaaeldin El-Nouby, Mido Assran, Nicolas Ballas, Wojciech Galuba, Russell Howes, Po-Yao Huang, Shang-Wen Li, Ishan Misra, Michael Rabat, Vasu Sharma, Gabriel Synnaeve, Hu Xu, Herve Jegou, Julien Mairal, Patrick Labatut, Armand Joulin, and Piotr Bojanowski. DINOv2: Learning Robust Visual Features without Supervision. *TMLR*, 2024. 1, 2, 3, 4, 8, 12
- [34] Aljosa Osep, Tim Meinhardt, Francesco Ferroni, Neehar Peri, Deva Ramanan, and Laura Leal-Taixé. Better Call SAL: Towards Learning to Segment Anything in Lidar. In *ECCV*, 2024. 3
- [35] Songyou Peng, Kyle Genova, Chiyu "Max" Jiang, Andrea Tagliasacchi, Marc Pollefeys, and Thomas Funkhouser. Pointconv: Deep Convolutional Networks on 3D Point Clouds. In *CVPR*, 2019. 2
- [36] Songyou Peng, Kyle Genova, Chiyu "Max" Jiang, Andrea Tagliasacchi, Marc Pollefeys, and Thomas Funkhouser. OpenScene: 3D Scene Understanding with Open Vocabularies. In *CVPR*, 2023. 3, 5
- [37] Gilles Puy, Spyros Gidaris, Alexandre Boulch, Oriane Siméoni, Corentin Sautier, Patrick Pérez, Andrei Bursuc, and Renaud Marlet. Three Pillars Improving Vision Foundation Model Distillation for Lidar. In *CVPR*, 2024. 3
- [38] Charles R Qi, Hao Su, Kaichun Mo, and Leonidas J Guibas. PointNet: Deep Learning on Point Sets for 3D Classification and Segmentation. In *CVPR*, 2017. 2
- [39] Charles Ruizhongtai Qi, Li Yi, Hao Su, and Leonidas J Guibas. PointNet++: Deep Hierarchical Feature Learning on Point Sets in a Metric Space. In *NeurIPS*, 2017. 2
- [40] Guocheng Qian, Yuchen Li, Houwen Peng, Jinjie Mai, Hasan Hammoud, Mohamed Elhoseiny, and Bernard Ghanem. PointNeXt: Revisiting PointNet++ with Improved Training and Scaling Strategies. In *NeurIPS*, 2022. 6
- [41] Alec Radford, Jong Wook Kim, Chris Hallacy, Aditya Ramesh, Gabriel Goh, Sandhini Agarwal, Girish Sastry, Amanda Askell, Pamela Mishkin, Jack Clark, et al. Learning Transferable Visual Models From Natural Language Supervision. In *ICML*, 2021. 1, 3
- [42] Damien Robert, Bruno Vallet, and Loic Landrieu. Learning Multi-View Aggregation In the Wild for Large-Scale 3D Semantic Segmentation. In *CVPR*, 2022. 2, 3, 6
- [43] Robin Rombach, Andreas Blattmann, Dominik Lorenz, Patrick Esser, and Björn Ommer. High-Resolution Image Synthesis With Latent Diffusion Models. In *CVPR*, 2022. 1
- [44] David Rozenberszki, Or Litany, and Angela Dai. Language-Grounded Indoor 3D Semantic Segmentation in the Wild. In *ECCV*, 2022. 1, 2, 5, 12
- [45] Corentin Sautier, Gilles Puy, Spyros Gidaris, Alexandre Boulch, Andrei Bursuc, and Renaud Marlet. Image-to-Lidar Self-Supervised Distillation for Autonomous Driving Data. In *CVPR*, 2022. 3
- [46] Christoph Schuhmann, Richard Vencu, Romain Beaumont, Robert Kaczmarczyk, Clayton Mullis, Aarush Katta, Theo Coombes, Jenia Jitsev, and Aran Komatsuzaki. LAION-400M: Open Dataset of CLIP-Filtered 400 Million Image-Text Pairs. *arXiv preprint arXiv:2111.02114*, 2021. 1
- [47] Christoph Schuhmann, Romain Beaumont, Richard Vencu, Cade Gordon, Ross Wightman, Mehdi Cherti, Theo Coombes, Aarush Katta, Clayton Mullis, Mitchell Wortsman, et al. LAION-5B: An Open Large-Scale Dataset for Training Next Generation Image-Text Models. *NeurIPS*, 2022. 1
- [48] Leslie N. Smith and Nicholay Topin. Super-Convergence: Very Fast Training of Neural Networks Using Large Learning Rates. In *Artificial Intelligence and Machine Learning for Multi-Domain Operations Applications*, 2019. 12
- [49] Andreas Peter Steiner, Alexander Kolesnikov, Xiaohua Zhai, Ross Wightman, Jakob Uszkoreit, and Lucas Beyer. How to train your ViT? Data, Augmentation, and Regularization in Vision Transformers. *TMLR*, 2022. 8
- [50] Pei Sun, Henrik Kretzschmar, Xerxes Dotiwalla, Aurelien Chouard, Vijaysai Patnaik, Paul Tsui, James Guo, Yin Zhou, Yuning Chai, Benjamin Caine, Vijay Vasudevan, Wei Han, Jiquan Ngiam, Hang Zhao, Aleksei Timofeev, Scott Ettinger, Maxim Krivokon, Amy Gao, Aditya Joshi, Yu Zhang, Jonathon Shlens, Zhifeng Chen, and Dragomir Anguelov. Scalability in Perception for Autonomous Driving: Waymo Open Dataset. In *CVPR*, 2020. 1, 3, 5, 12
- [51] Mingkui Tan, Zhuangwei Zhuang, Sitao Chen, Rong Li, Kui Jia, Qicheng Wang, and Yuanqing Li. EPMF: Efficient perception-aware multi-sensor fusion for 3D semantic segmentation. *IEEE TPAMI*, 2024. 2, 3
- [52] Haotian Tang, Zhijian Liu, Shengyu Zhao, Yujun Lin, Ji Lin, Hanrui Wang, and Song Han. Searching Efficient 3D Architectures with Sparse Point-Voxel Convolution. In *ECCV*, 2020. 6
- [53] Hugues Thomas, Charles R Qi, Jean-Emmanuel Deschaud, Beatriz Marcotegui, François Goulette, and Leonidas J Guibas. KPConv: Flexible and Deformable Convolution for Point Clouds. In *CVPR*, 2019. 2
- [54] Michael Tschannen, Alexey Gritsenko, Xiao Wang, Muhammad Ferjad Naeem, Ibrahim Alabdulmohsin, Nikhil Parthasarathy, Talfan Evans, Lucas Beyer, Ye Xia, Basil Mustafa, et al. SigLIP 2: Multilingual Vision-Language Encoders with Improved Semantic Understanding, Localization, and Dense Features. *arXiv preprint arXiv:2502.14786*, 2025. 5, 8
- [55] Peng-Shuai Wang. OctFormer: Octree-based Transformers

- for 3D Point Clouds. *ACM Transactions on Graphics (SIG-GRAPH)*, 42(4), 2023. [2](#), [6](#)
- [56] Xiaoyang Wu, Yixing Lao, Li Jiang, Xihui Liu, and Hengshuang Zhao. Point Transformer V2: Grouped Vector Attention and Partition-based Pooling. In *NeurIPS*, 2022. [1](#), [2](#), [6](#)
- [57] Xiaoyang Wu, Xin Wen, Xihui Liu, and Hengshuang Zhao. Masked Scene Contrast: A Scalable Framework for Unsupervised 3D Representation Learning. In *CVPR*, 2023. [7](#)
- [58] Xiaoyang Wu, Li Jiang, Peng-Shuai Wang, Zhijian Liu, Xihui Liu, Yu Qiao, Wanli Ouyang, Tong He, and Hengshuang Zhao. Point Transformer V3: Simpler, Faster, Stronger. In *CVPR*, 2024. [1](#), [2](#), [4](#), [5](#), [6](#), [7](#), [8](#), [12](#), [19](#), [20](#), [21](#)
- [59] Xiaoyang Wu, Zhuotao Tian, Xin Wen, Bohao Peng, Xihui Liu, Kaicheng Yu, and Hengshuang Zhao. Towards Large-scale 3D Representation Learning with Multi-dataset Point Prompt Training. In *CVPR*, 2024. [2](#), [5](#), [7](#)
- [60] Xu Yan, Jiantao Gao, Chaoda Zheng, Chao Zheng, Ruimao Zhang, Shuguang Cui, and Zhen Li. 2DPASS: 2D Priors Assisted Semantic Segmentation on LiDAR Point Clouds. In *ECCV*, 2022. [3](#), [6](#)
- [61] Chaolong Yang, Yuyao Yan, Weiguang Zhao, Jianan Ye, Xi Yang, Amir Hussain, Bin Dong, and Kaizhu Huang. Towards Deeper and Better Multi-view Feature Fusion for 3D Semantic Segmentation. In *International Conference on Neural Information Processing*, 2023. [6](#)
- [62] Yu-Qi Yang, Yu-Xiao Guo, Jian-Yu Xiong, Yang Liu, Hao Pan, Peng-Shuai Wang, Xin Tong, and Baining Guo. Swin3D: A Pretrained Transformer Backbone for 3D Indoor Scene Understanding. *arXiv preprint arXiv:2304.06906*, 2023. [2](#), [6](#)
- [63] Kadir Yilmaz, Jonas Schult, Alexey Nekrasov, and Bastian Leibe. Mask4Former: Mask Transformer for 4D Panoptic Segmentation. In *ICRA*, 2024. [2](#)
- [64] Xiaohua Zhai, Basil Mustafa, Alexander Kolesnikov, and Lucas Beyer. Sigmoid Loss for Language Image Pre-Training. In *ICCV*, 2023. [1](#)
- [65] Zhiwei Zhang, Zhizhong Zhang, Qian Yu, Ran Yi, Yuan Xie, and Lizhuang Ma. LiDAR-Camera Panoptic Segmentation via Geometry-Consistent and Semantic-Aware Alignment. In *ICCV*, 2023. [2](#), [3](#), [6](#)
- [66] Hengshuang Zhao, Li Jiang, Jiaya Jia, Philip HS Torr, and Vladlen Koltun. Point Transformer. In *ICCV*, 2021. [2](#), [6](#)
- [67] Jia Zheng, Junfei Zhang, Jing Li, Rui Tang, Shenghua Gao, and Zihan Zhou. Structured3D: A Large Photo-realistic Dataset for Structured 3D Modeling. In *ECCV*, 2020. [1](#), [6](#), [12](#)
- [68] Xinge Zhu, Hui Zhou, Tai Wang, Fangzhou Hong, Yuexin Ma, Wei Li, Hongsheng Li, and Dahua Lin. Cylindrical and Asymmetrical 3D Convolution Networks for LiDAR Segmentation. In *CVPR*, 2021. [4](#), [6](#)
- [69] Zhuangwei Zhuang, Rong Li, Kui Jia, Qicheng Wang, Yuanqing Li, and Mingkui Tan. Perception-Aware Multi-Sensor Fusion for 3D LiDAR Semantic Segmentation. In *ICCV*, 2021. [3](#)

A. Implementation Details

Our implementation builds upon PTv3 [58]. As such, we use the same hyperparameter settings wherever possible. However, unlike PTv3, DITR also utilizes images, for which we add image-specific augmentations. Below, we provide detailed implementation settings for each dataset.

Indoor Semantic Segmentation. Following PTv3, the model is trained with a batch size of 12 for 800 epochs on ScanNet [8] and ScanNet200 [44], and for 3000 epochs on the smaller S3DIS [1] dataset. Optimization is performed using the AdamW [30] optimizer, with a 1cycle [48] learning rate schedule. The maximum learning rate is set to 6×10^{-3} with the learning rate peaking at 5% of the training process. Point cloud augmentations include random rotation, random dropout of points, random scaling, random flipping, elastic distortion, and color jittering. Grid sampling is applied with a grid size of 2 cm.

Before being fed into DINOv2 [33], ScanNet images are resized to 420×560 pixels while S3DIS images are resized to 518×518 pixels, preserving the aspect ratio and ensuring a comparable number of image tokens to those used during DINOv2 training. Images undergo augmentation with random horizontal flipping and color jittering. During training, 10 images are randomly selected per 3D scene, while during validation, 10 temporally equidistant images are chosen for consistent evaluation.

We only inject features for points that are visible in the selected images. To prevent injecting features for occluded points, we compare the depth of each projected point with the raw depth value from the RGB-D sensor and exclude points where the depth difference exceeds a small margin of error. Additionally, to ensure that image features consistently are assigned to points at similar distances, points that are closer than 1 m or farther than 4 m are filtered out. Given that the 3D scene is captured from multiple camera angles with overlapping regions, most points fall in this range in at least one image.

When distilling DINOv2 [33] features into the 3D model, the ScanNet [8] and Structured3D [67] datasets are used for joint training. Each batch consists of samples from only one dataset, with half of the batches derived from ScanNet and the other half from Structured3D. We train the model for a total of 160k steps with a batch size of 12. After distillation, the pretrained model is fine-tuned separately on the ScanNet, ScanNet200, and S3DIS datasets. For ScanNet and S3DIS, the model is fine-tuned for 10% of the default number of epochs, and, except for the segmentation head, the learning rate is set to 10% of its original value. For ScanNet200, fine-tuning is performed using the default training setup described earlier. This approach reflects differences in dataset complexity: ScanNet and S3DIS, with

fewer classes, achieve strong performance with minimal fine-tuning, while ScanNet200, which has a larger and more challenging class set, benefits from longer training to fully utilize the model’s capacity.

Outdoor Semantic Segmentation. Following PTv3, the model is trained with a batch size of 12 for 50 epochs on nuScenes [4], SemanticKITTI [3] and Waymo [50]. Again, optimization is performed using the AdamW optimizer, with a 1cycle learning rate schedule. The maximum learning rate is set to 2×10^{-3} with the learning rate peaking at 4% of the training process. Point cloud augmentations include random rotation, random scaling, and random flipping. Grid sampling is performed with a grid size of 5 cm.

To obtain DINOv2 features, nuScenes [4] images are resized to 378×672 pixels, SemanticKITTI [3] to 378×1246 , and Waymo [50] to 308×672 . This keeps the original aspect ratios while also yielding a number of image tokens similar to what was used during DINOv2’s training. We make an exception for the wide-aspect-ratio images in SemanticKITTI, using a higher resolution to avoid excessively reducing the vertical resolution. As with the indoor datasets, images undergo random horizontal flipping and color jittering augmentations.

For distillation, we jointly train the model on the nuScenes, SemanticKITTI, and Waymo datasets. Each batch consists of samples of one dataset and batches are equally distributed across the datasets. We train the model for a total of 350k steps with a batch size of 12. After distillation, the pretrained model is fine-tuned separately on nuScenes, SemanticKITTI, and Waymo. For the SemanticKITTI dataset, the model is fine-tuned for 10% of the default number of epochs and, except for the segmentation head, the learning rate is set to 10% of its original value. For nuScenes and Waymo, fine-tuning is performed using the default training setup described earlier.

B. Qualitative Results

Distillation. We apply Principal Component Analysis (PCA) to the point features generated by the distilled D-DITR model and visualize the first three principal components as RGB colors. This provides a qualitative view of the semantic information captured during distillation pre-training. Note that this model operates without image input during inference.

Figures 4 to 8 highlight the rich semantic features distilled from DINOv2. Points belonging to the same semantic class exhibit similar colors, reflecting alignment along the first three principal axes. For instance, in Figs. 4 and 5, objects such as tables, chairs, books, and walls consistently map to distinct colors across the scene. These results show that the model captures fine-grained semantic representations of 3D scenes without requiring semantic labels during

training. Furthermore, Figs. 4 and 5 reveal that objects like chairs and tables are segmented into finer subparts in feature space, surpassing the granularity of the dataset annotations. This semantically rich feature representation significantly enhances the model’s performance for semantic segmentation fine-tuning, as is evident by the quantitative results in the main paper.

Semantic Segmentation. Figures 9 to 11 compare the predictions of DITR and PTV3, with a focus on points where DITR benefits from DINOv2 features.

In Fig. 9, we observe that PTV3 misclassifies a ‘cart’ as a ‘shelf’ due to the structural similarities between these classes in the 3D point cloud. In contrast, DITR accurately identifies the carts by incorporating visual cues from 2D images via DINOv2 feature injection.

In Fig. 10 we show another perspective of the same scene. Here, PTV3 misclassifies a ‘cabinet’ as a ‘wall’, as the cabinet appears as a flat surface that is flush with the wall and has a similar color, making it almost impossible to identify it as a cabinet based on the point cloud only. However, DITR correctly classifies the cabinet, as it is clearly visible in one of the image views. This highlights how leveraging strong image features can complement and enhance geometric features, enabling the model to differentiate between structurally similar classes.

Finally, in Fig. 11, we present an example from the nuScenes dataset. PTV3 misclassifies a pedestrian crossing the street as a car, overlooks several pedestrians on the sidewalk, and confuses a bus with a building. These errors occur in areas distant from the ego vehicle, where LiDAR data is sparse, and objects are represented by only a few points. In contrast, DITR accurately predicts these instances, leveraging contextual information from the respective image for disambiguation.

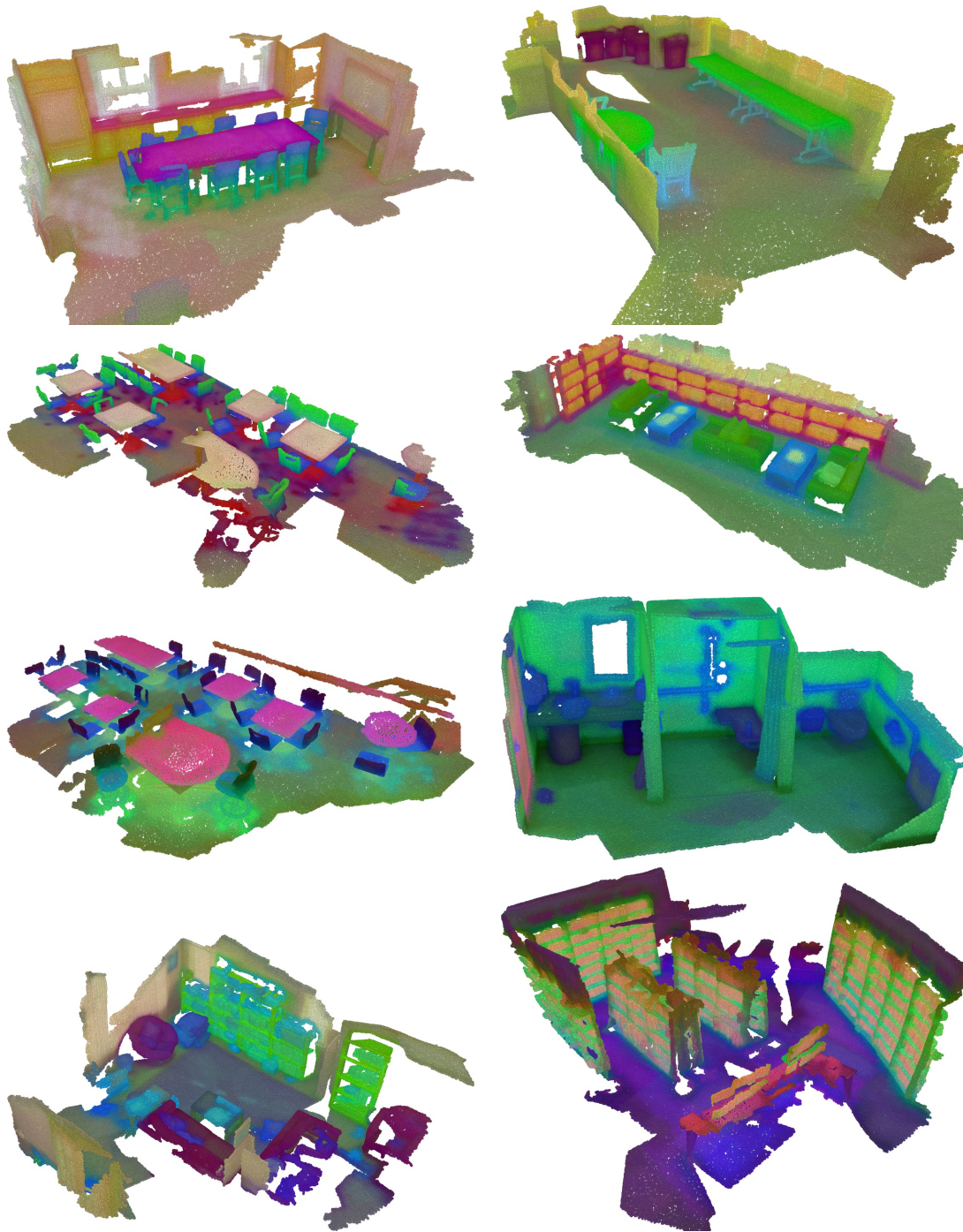


Figure 4. **PCA visualization of distilled D-DITR features for ScanNet [8].** We visualize the first three principal components of the point features learned by the D-DITR model. PCA projections are computed per scene and hence there is no correspondence of colors between figures.

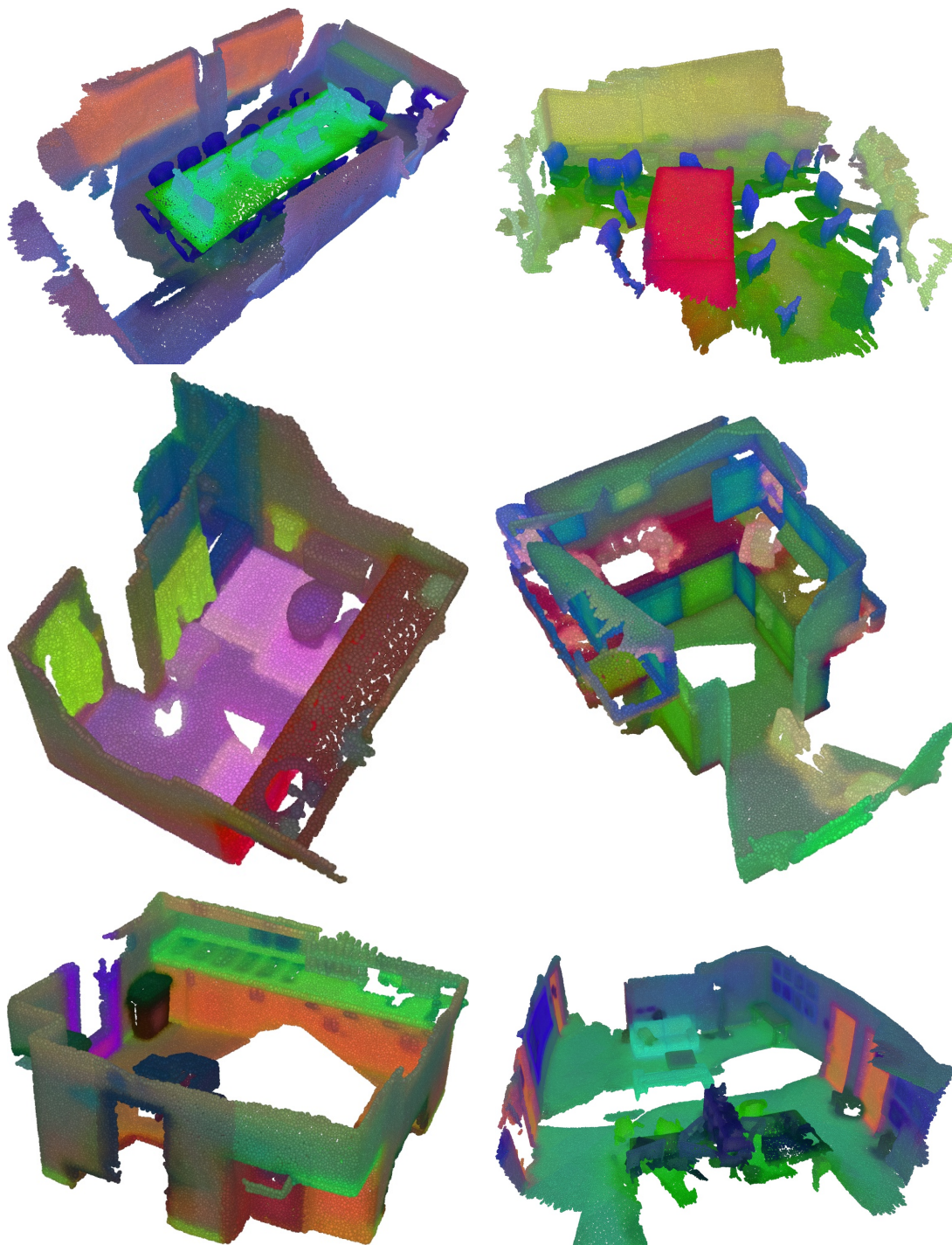


Figure 5. (Cont.) PCA visualization of distilled D-DITR features for ScanNet [8]. We visualize the first three principal components of the point features learned by the D-DITR model. PCA projections are computed per scene and hence there is no correspondence of colors between figures.

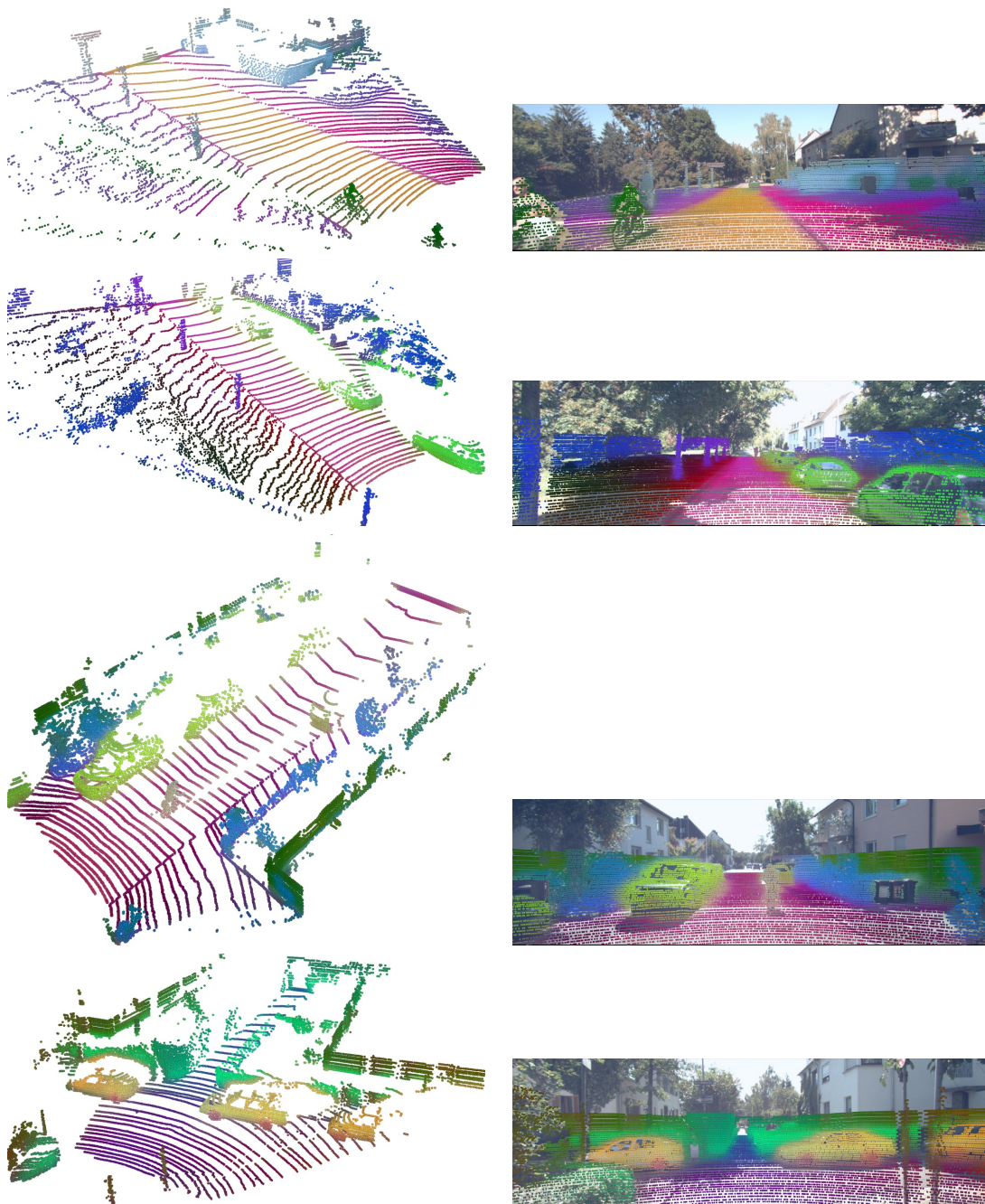


Figure 6. **PCA visualization of distilled D-DITR features for SemanticKITTI [3].** We visualize the first three principal components of the point features learned by the D-DITR model (left), as well as the corresponding 2D projections (right).

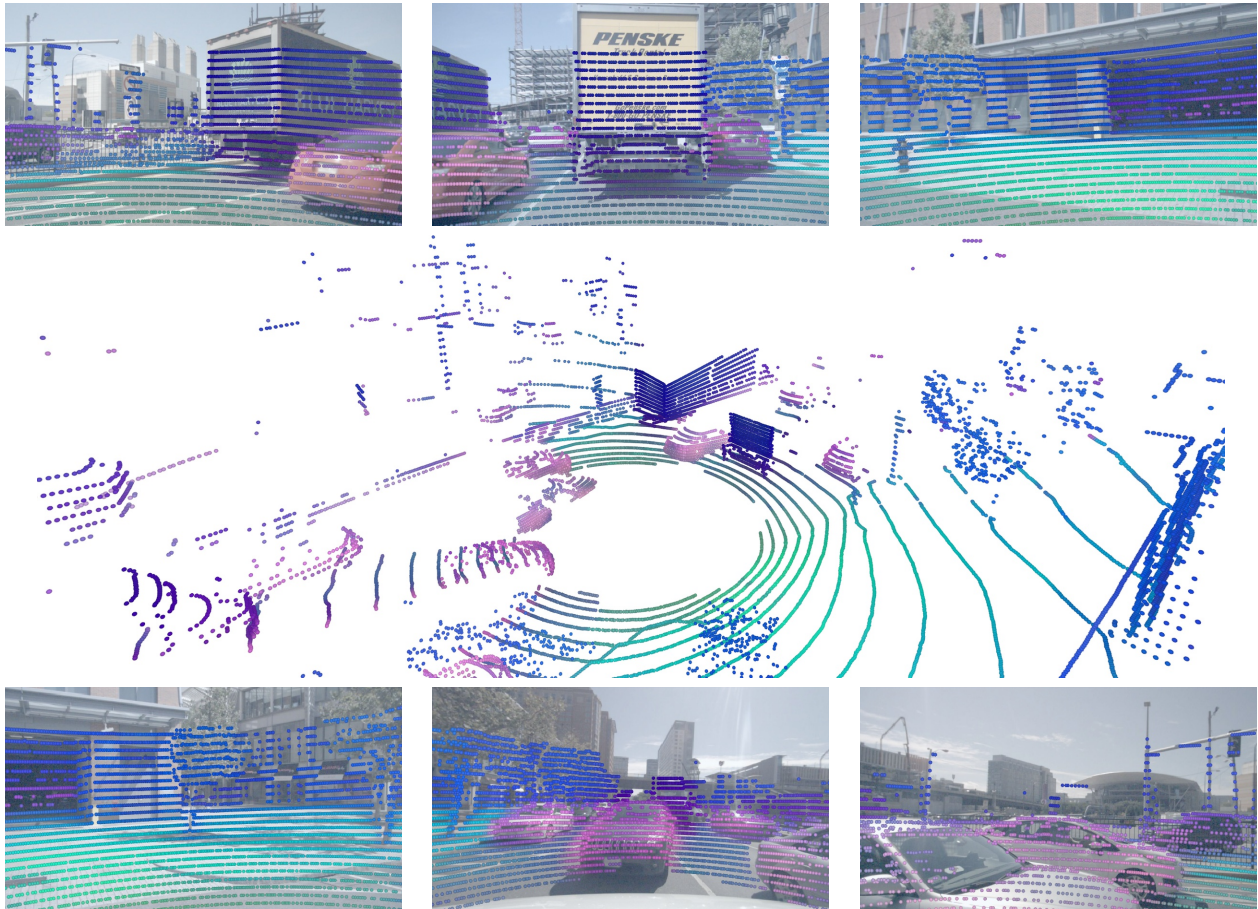


Figure 7. **PCA visualization of distilled D-DITR features for nuScenes [4].** We visualize the first three principal components of the point features learned by the D-DITR model.

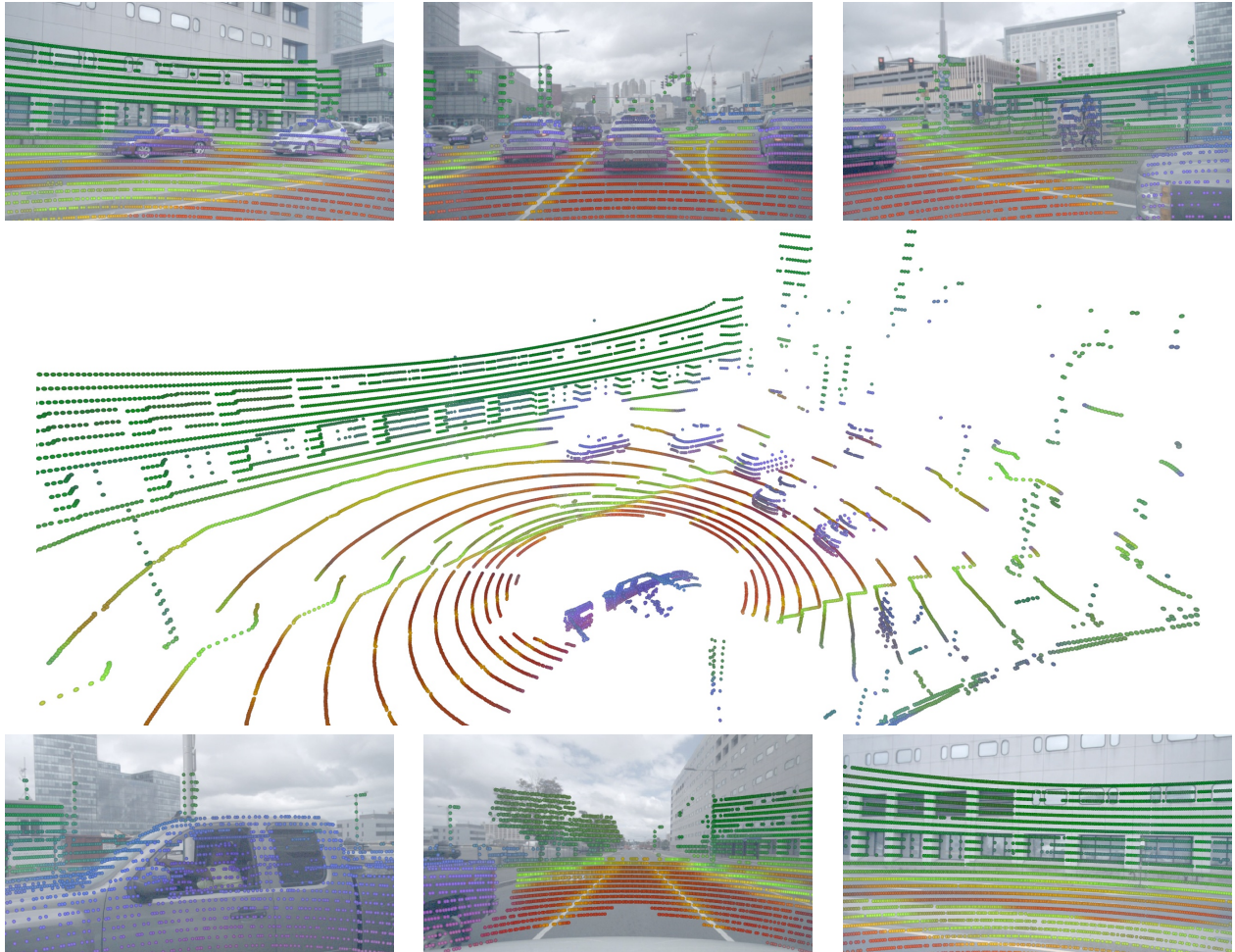
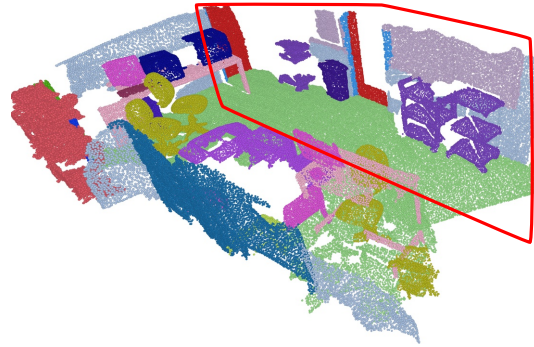


Figure 8. **PCA visualization of distilled D-DITR features for nuScenes [4].** We visualize the first three principal components of the point features learned by the D-DITR model.



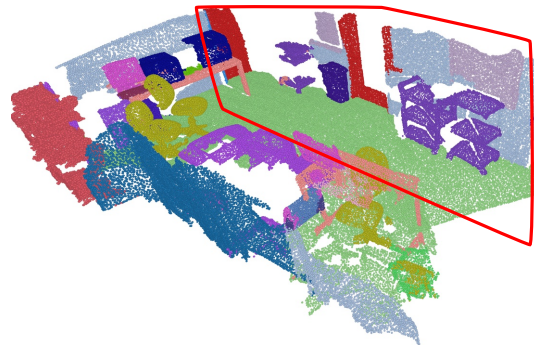
2D projected ground truth



Full 3D ground truth



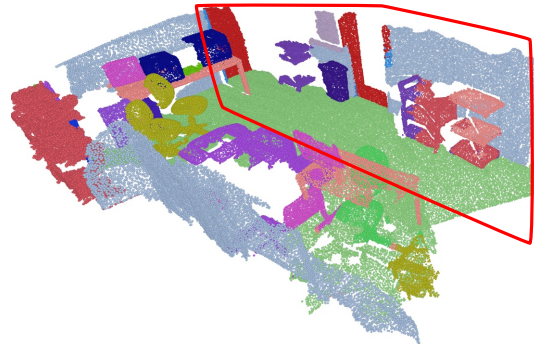
2D projected DITR predictions



Full 3D DITR predictions



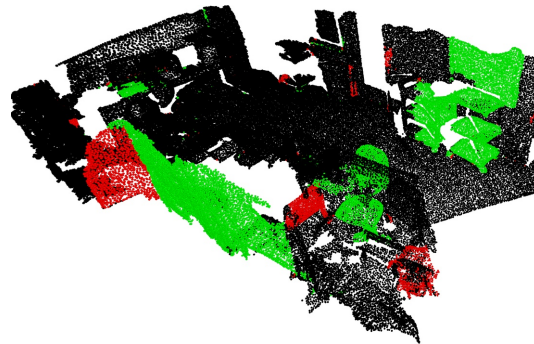
2D projected PTV3 predictions



Full 3D PTV3 predictions



3D point cloud input

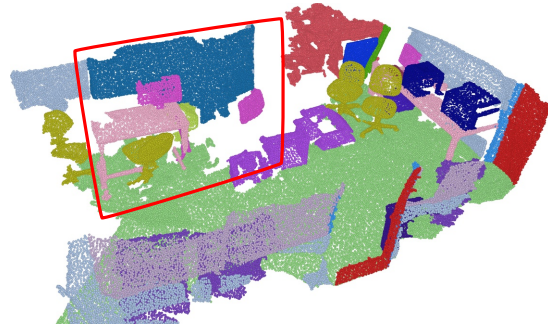


Difference between PTV3 and DITR predictions

Figure 9. **DITR and PTV3 [58] segmentation for ScanNet [8].** The wheels of the cart are barely visible in the 3D point cloud, hence likely causing PTV3 to misclassify it as a shelf. The bottom-right visualization illustrates the differences between PTV3 and DITR predictions. Points where both methods are correct or both are incorrect are shown in black. Points correctly predicted by only one method are color-coded: green for DITR and red for PTV3.



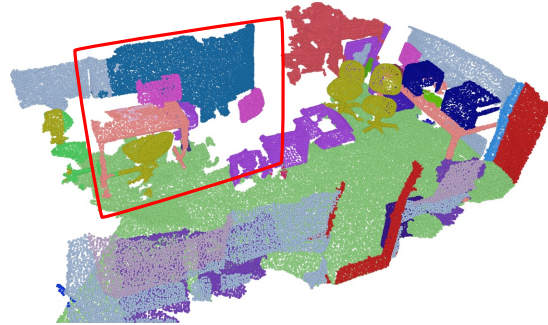
2D projected ground truth



Full 3D ground truth



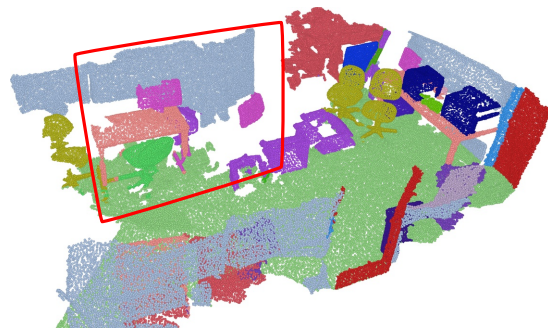
2D projected DITR predictions



Full 3D DITR predictions



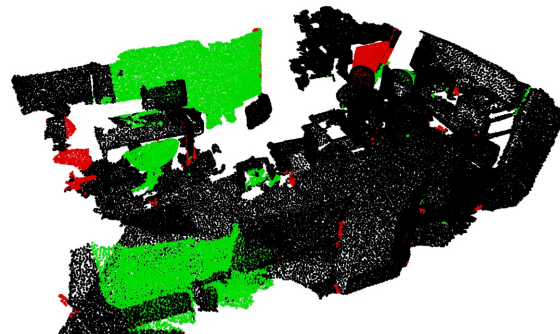
2D projected PTv3 predictions



Full 3D PTv3 predictions



3D point cloud input



Difference between PTv3 and DITR predictions

Figure 10. **DITR and PTv3 [58] semantic segmentation for ScanNet [8]**. In the 3D point cloud, the cabinet at the back appears as a flat surface flush with the wall, leading PTv3 to misclassify it as part of the wall. However, in the corresponding image, this region is clearly identifiable as a cabinet. The bottom-right visualization illustrates the differences between PTv3 and DITR predictions. Points where both methods are correct or both are incorrect are shown in black. Points correctly predicted by only one method are color-coded: green for DITR and red for PTv3.

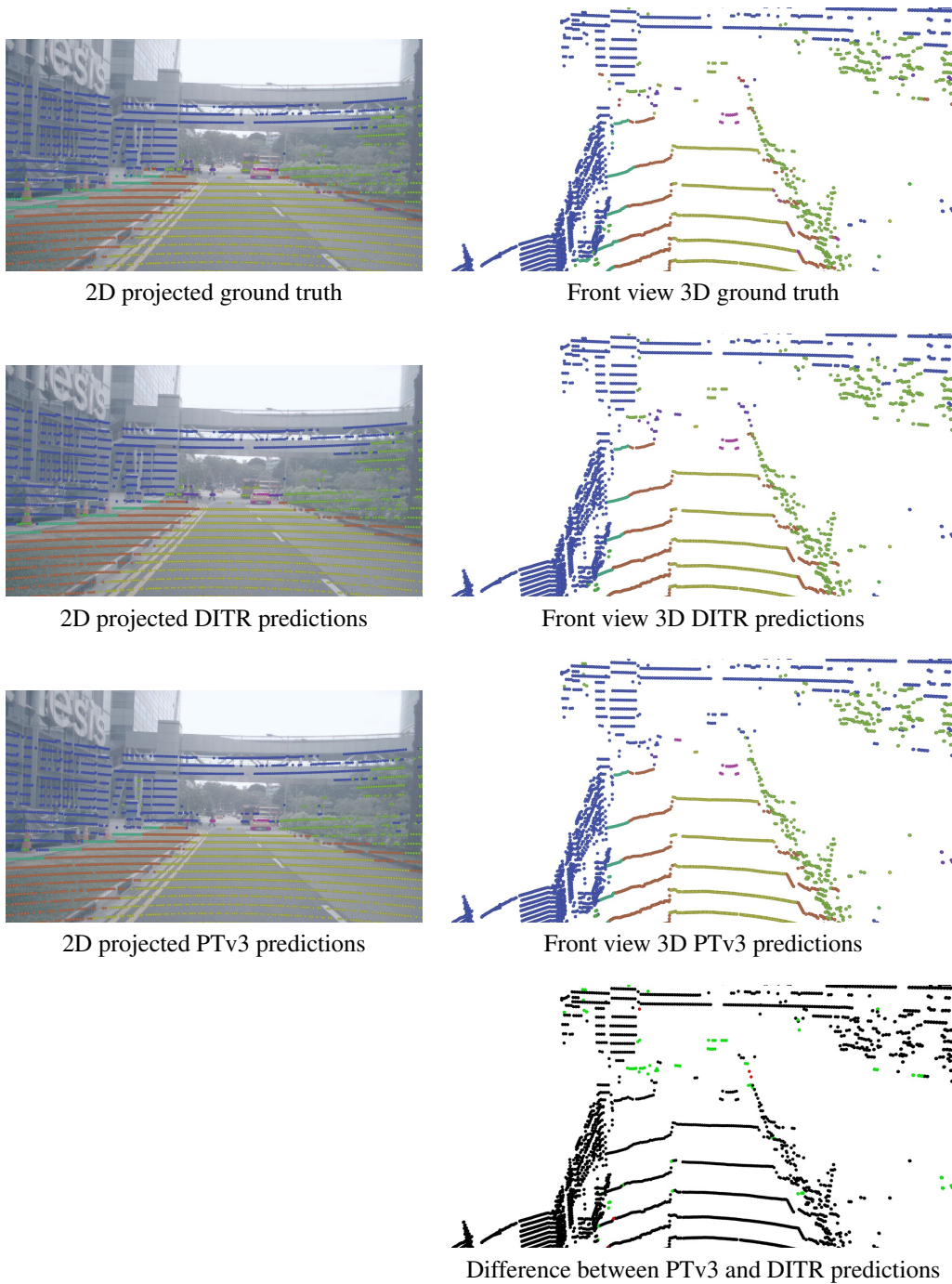


Figure 11. **DITR and PTV3 [58] semantic segmentation for nuScenes [4]**. PTV3 misclassifies the pedestrian crossing the street as a car, overlooks the pedestrians on the left sidewalk and the pedestrian on the right, and mistakes the bus in front of the car for a building. These errors occur in areas distant from the ego vehicle, where LiDAR data is sparse, and objects are represented by only a few points. In contrast, DITR can leverage the corresponding image, where the bus and pedestrian on the street are clearly visible, allowing it to make the correct predictions despite the objects being represented by only a few points. The bottom-right visualization illustrates the differences between PTV3 and DITR predictions. Points where both methods are correct or both are incorrect are shown in black. Points correctly predicted by only one method are color-coded: green for DITR and red for PTV3.